


## Spintronic Terahertz Emitters in Silicon-Based Heterostructures

Jiayun Liu<sup>1,§</sup>, Kyusup Lee<sup>2,§</sup>, Yingshu Yang<sup>1</sup>, Ziqi Li<sup>1</sup>, Raghav Sharma<sup>2</sup>, Lifei Xi<sup>3</sup>,  
Teddy Salim<sup>3</sup>, Chris Boothroyd<sup>3</sup>, Yeng Ming Lam<sup>3</sup>, Hyunsoo Yang<sup>2,\*</sup>, Marco Battiato<sup>1,†</sup> and  
Elbert E.M. Chia<sup>1,‡</sup>

<sup>1</sup>*Division of Physics and Applied Physics, School of Physical and Mathematical Sciences, Nanyang Technological University, 21 Nanyang Link, 637371, Singapore*

<sup>2</sup>*Department of Electrical and Computer Engineering, National University of Singapore, 117576, Singapore*

<sup>3</sup>*School of Materials Science and Engineering Nanyang Technological University 50 Nanyang Avenue, 639798, Singapore*

 (Received 11 February 2022; revised 7 July 2022; accepted 19 August 2022; published 21 September 2022)

Integration of active elements into silicon wafers is the first step towards their usage in modern electronic devices based on nanometric structures. Spintronic terahertz emitters, typically composed of nanometer-thin magnetic multilayer, have the outstanding capability of producing high-quality, broadband terahertz pulses using extremely simple heterostructures. A question remains on whether an efficient and cheap integration with other silicon-based technologies can be achieved. We show here that simply having a ferromagnetic layer on silicon produces remarkably efficient spintronic terahertz emission despite the low spin-orbit coupling of the individual components. We achieve this by leveraging on the natural formation of silicides at the interface of a transition metal and silicon. The cobalt silicide layer has good spin-to-charge conversion efficiency that reaches around 1/6 as that of the prototypical spintronics THz-emitter heterostructure cobalt/platinum.

DOI: [10.1103/PhysRevApplied.18.034056](https://doi.org/10.1103/PhysRevApplied.18.034056)

### I. INTRODUCTION

Terahertz (THz) radiation covers a highly attractive frequency range corresponding to phonon resonances [1,2] as well as the characteristic energy of molecular motion [3] of many materials. Besides application in conventional pump-probe THz spectroscopy, THz has seen an increase in research interest across areas like life sciences [4] and material characterization like two-dimensional (2D) materials [5–7] and topological materials [8,9]. Despite its wide application, the scientific and technological application of THz radiation is not as mature as the neighboring frequency ranges (radio and infrared). The steady improvement in the techniques used to produce THz radiation [10–12] have helped close the so-called THz gap and driven a steady growth of the usage of THz radiation not only in many research areas, but also commercial applications [11,13–15]. There is however one aspect where the THz gap still remains open. There are currently available technologies that integrate radio and infrared radiation

generators into silicon. However, the same integration is lacking in the case of THz generators.

The millimeter-thick nonlinear crystals typically used for efficient THz generation have limited the integration with modern microprocessors. This, together with the narrow bandwidth [16], prompts for the search for alternative THz generation methods. Fortunately, the recent progress in the field of spintronics has brought about the realization of spintronic THz emitter [17]. This is typically made from a heterostructure consisting of a ferromagnetic (FM) and a nonmagnetic (NM) metal layer, where the emitted THz intensity is comparable with that from mm-size nonlinear crystals [18]. These nm-thick spintronic THz emitters [16] have gained a lot of popularity due to broad bandwidth, flexibility in the optimization and integration into more complex devices [19], thus offering the possibility of integration with microprocessors [20]. This is especially useful for the next-generation devices as transistors are approaching the quantum limit and devices are pushing their performance through transistor stacking [21].

Despite the attractiveness of spintronic THz emitters, the integration with Si is nontrivial due to silicide formation at the interface. It is known that silicides are formed at the interface of transition metal layers and silicon [22,23]. Although silicides have traditionally been used to interface metal and semiconductors to reduce contact resistance

\*eleyang@nus.edu.sg

†marco.battiato@ntu.edu.sg

‡elbertchia@ntu.edu.sg

§These authors contributed equally to this work.

[24,25], it is considered detrimental for spin-based applications, since the silicide can be magnetic [26], and so offers magnetic scattering sites leading to spin-flip scattering [27] and the destruction of spin polarization of the electrons. A previous photoemission measurement [26] reported the formation of cobalt silicide with different stoichiometry in Co/Si interfaces that are both magnetic (e.g.,  $\text{Co}_3\text{Si}$ ) and nonmagnetic (e.g.,  $\text{Co}_2\text{Si}$ ,  $\text{CoSi}$ , and  $\text{CoSi}_2$ ).

Considering the central role that silicon plays in modern electronics, it is therefore advantageous to integrate a spintronics THz emitter with silicon to create optoelectronics devices at THz frequencies. In this paper, we present the THz emission from Co/Si heterostructure and show the production of sizeable THz radiation comparable to other known efficient bilayers like Co/W and Co/Pt. We identify the silicide layer formed at the interface as responsible for the large spin-to-charge conversion. This suggests that integration of spintronics THz emitters into silicon electronics can be achieved with emitted powers, which are sufficient for technological applications.

## II. EXPERIMENT

### A. Sample fabrication

All thin films are deposited using sputtering techniques on top of quartz substrates. The quartz substrates are cleaned with acetone and isopropanol for 10 min each in an ultrasonicator before sputtering. For the Si/Co bilayers, the Si layer is first deposited using magnetron sputtering at a base pressure below  $1.0 \times 10^{-7}$  Torr (Kert J. Lesker Co.). The Si sputter target is nondoped and its purity is as high as 99.999% (ACI alloys). The deposition is carried out using a rf power of 60 W on the target and with Ar gas at a pressure of 3 mTorr. The various Si thicknesses ( $d = 0, 2, 4, 6, 8,$  and  $10$  nm) are prepared at a sputtering rate of approximately 3 nm/min. Subsequently, the as-deposited Si thin films are transferred directly to a magnetron sputtering chamber (AJA Int. Inc). The 3-nm-thick Co deposition is carried out at a base pressure below  $5 \times 10^{-9}$  Torr, using a dc power of 60 W and with Ar gas at a pressure of 3 mTorr. The Co sputtering rate is as fast as approximately 1 nm/min. For the heavy metal/Si/Co trilayers, the Pt or W layer is first deposited using a dc power of 60 W and with Ar gas at pressure of 2 mTorr (AJA Int. Inc), which is followed by the Si and Co deposition. All thin films are encapsulated with the 3-nm-thick  $\text{SiO}_2$  layer using the rf sputtering in the magnetron sputtering chamber.

### B. Experimental setup

A Ti:sapphire regenerative amplifier (Coherent Legend) with 800-nm central wavelength, pulse duration of 30 fs, and repetition rate of 1 kHz is used for the experiment. The beam is split into a pump beam and a gating beam for THz detection using EO sampling. The pump beam is normal

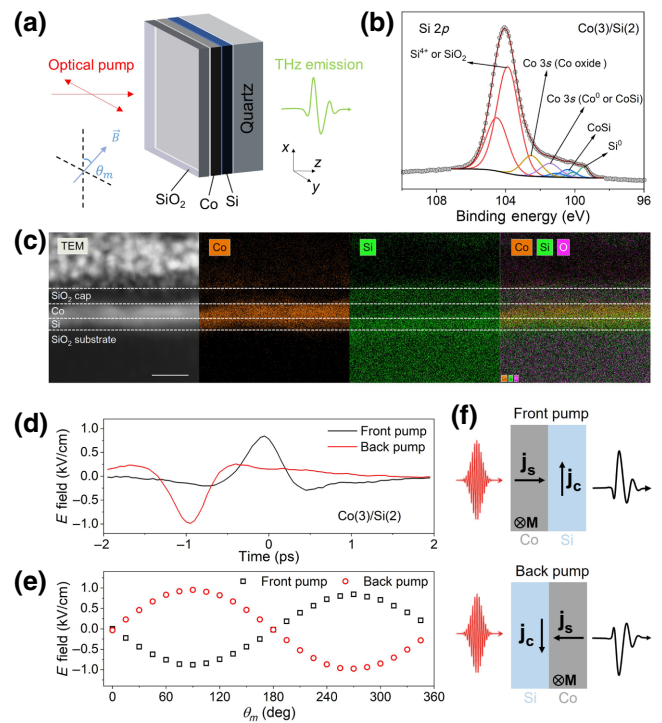


FIG. 1. (a) Schematic of excitation and THz emission from  $\text{SiO}_2$  (3 nm)/Co (3 nm)/Si (2 nm)/quartz substrate (1 mm). The direction of the applied magnetic field is denoted by  $\theta_m$ . (b) XPS spectrum and (c) cross-section TEM and EDX image of Co(3 nm)/Si(2 nm). The white scale bar is 5 nm. (d) Emitted THz waveform from front (black) and back (red) pump, showing a flip in polarity of THz waveform when pump direction is reversed. (e) Peak THz  $E$ -field versus  $B$ -field direction for front (black) and back (red) pump, showing onefold dependence. (f) Reversal of spin current ( $\mathbf{j}_s$ ) and charge current ( $\mathbf{j}_c$ ) due to flipping of sample. The data in (d),(e) imply the SCC conversion mechanism in Co/Si.

incident onto the capping layer side of the sample as shown in Fig. 1(a). Residual pump beam after the sample is filtered out by a high-density polyethylene filter that is highly transmissive for THz waves. A linear polarizer for THz is placed behind the polyethylene filter with the transmission axis along  $\hat{x}$  such that only THz along the  $x$  axis is detected. The linearly polarized THz and the gating beam are both focused on a 1-mm-thick (110) ZnTe crystal. The gating beam is then separated into orthogonal polarization components by a Wollaston prism and detected by a balanced photodetector. An external magnetic field of approximately 800 Oe is applied to the sample to control the saturation magnetization direction of the Co layer. The absorbance measurement is measured at room temperature with a UV-VIS-NIR spectrophotometer (Perkin Elmer).

## III. RESULTS AND DISCUSSION

We prepare a set of Co(3 nm)/Si( $d$ ) bilayer thin films with varying Si thickness of  $d$  from 2–10 nm. Detailed

characterizations are performed to confirm the sample composition. Figure 1(b) shows the x-ray photoelectron spectroscopy (XPS) of the Co(3)/Si(2) sample, from which we conclude that the Si sample has mostly transformed to silicide in Co(3)/Si(2) (see the Supplemental Material [28] for more details). Figure 1(c) shows cross-section transmission electron microscopy (TEM) and energy-dispersive x-ray (EDX) mapping of the Co(3)/Si(2) sample. Here we focus on the Co, Si, O elements to distinguish the cap layer (Si and O elements), Co layer, Si layer, and quartz substrate (Si and O elements). From the elemental mapping images, we see that there is a clear overlap between Co and Si signals, further confirming that almost all Si has transformed to silicide in the Co(3)/Si(2) sample. Using XPS, TEM, EDX, and vibrating sample magnetometry (VSM, see the Supplemental Material [28]), we identify the silicide to be  $\text{Co}_x\text{Si}_y$  where  $x \approx y \approx 1$ . A 800-nm pump beam with the average power of 20 mW is focused on the capping layer side (“front pump”) of the sample at room temperature and normal incidence as shown in Fig. 1(a). The emitted THz passes through a linear polarizer and only the polarization direction parallel to the  $\hat{x}$  direction is transmitted and measured by electro-optic (EO) sampling.

In a spintronics THz emitter, the carriers in the FM layer are typically excited optically by an ultrashort laser pulse in the visible and near-infrared region, and thus bring the electrons into a nonequilibrium distribution and high-energy states [7]. Shortly after, the excited electrons undergo spin-dependent relaxation and transport in the FM producing a spin-polarized superdiffusive current [29,30]. This spin current  $\mathbf{j}_s$ , when injected in the NM layer, is converted into a charge current  $\mathbf{j}_c$  through either inverse Rashba-Edelstein effect (IREE) or inverse spin Hall effect (ISHE), or both, where the efficiency of the conversion is determined by the SOC (spin-orbit coupling) strength of the NM layer [31]. The induced  $\mathbf{j}_c$  typically has a time duration in the ps regime [17], which produces electromagnetic radiation in the THz range. Such a spin-to-charge conversion (SCC) mechanism obeys the relation  $\mathbf{j}_c \propto \mathbf{j}_s \times \mathbf{M}$  where  $\mathbf{j}_c$  is the charge current,  $\mathbf{j}_s$  is the spin current, and  $\mathbf{M}$  is the magnetization of the FM layer. The efficiency of conversion between the charge and spin current is given by the spin Hall angle  $\theta_{\text{SH}} = j_c/j_s$ .

To verify the origin of the emitted THz, the sample is pumped from the substrate side (“back pump”) while the external magnetic field is rotated along the  $x$ - $y$  plane. The magnetic field angle dependence measurement is taken at the peak THz field determined from the THz waveform. The one-fold sinusoidal dependence of the emitted THz amplitude on the magnetic field angle [Fig. 1(c)], as well as a change in polarity of the THz pulse for the front and back pump schemes [Fig. 1(b)], imply that SCC is the mechanism of the THz emission. The direction of optically driven spin current ( $\mathbf{j}_s$ ) in the Co layer is opposite for front and back pump schemes as depicted in Fig. 1(d).

The spin current is then injected into the adjacent Si layer and is converted into the transverse charge current ( $\mathbf{j}_c$ ), which results in the sign reversal of the emitted THz pulse [Fig. 1(b)]. This spin current dependence is also observed in reverse stacked samples (details in the Supplemental Material [28]). In addition, the injected spin polarization in the Si layer is controlled by the external magnetic field, and hence the direction of  $\mathbf{j}_c$  is manipulated by the external magnetic field direction [Fig. 1(c)]. Also, since the maximum and minimum values are approximately equal, it implies that the emitted THz is linearly polarized.

Since the spin Hall angle of Si is known to be negligibly small, it is expected to give negligible THz emission based on the SCC in the Si layer. However, the most surprising finding is that the peak THz radiation emitted from Co(3 nm)/Si(2 nm) [Fig. 1(b)] reaches around 1/6 in magnitude compared to that from a reference Co(3 nm)/Pt(6 nm) device, which is widely considered to have a high SCC efficiency, and even stronger than Co(3 nm)/W(6 nm) [Figs. 2(a) and 2(c)]. Such a remarkable result shows that a very efficient THz emitter can be created and integrated into a silicon device in the simplest possible geometry—by the simple addition of a Co layer. Next we show that a strong SCC happens within a thin metallic silicide layer formed at the Co/Si interface.

It is now a question of which type of silicide is formed and, whether it is the silicide that is responsible for the SCC. To characterize the silicide formation in our devices, we measure the absorbance spectra of Co(3 nm)/Si( $d$ ) and Si( $d$ ) for  $d = 2, 4, 6, 8, 10$  nm. We first analyze the squared

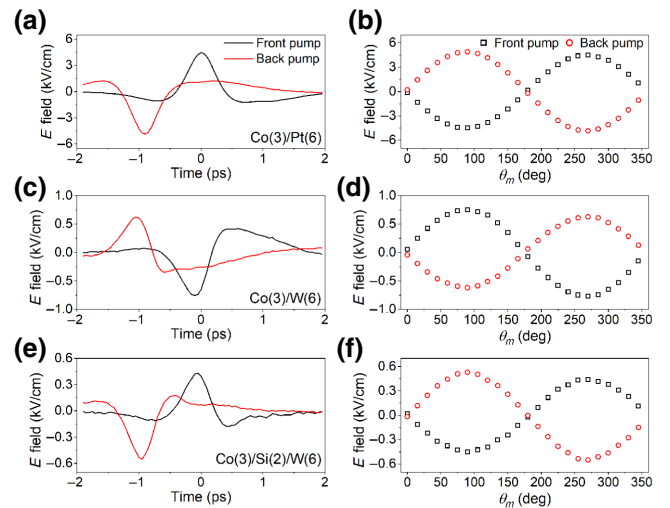


FIG. 2. THz emission data of (a),(b) Co(3 nm)/Pt(6 nm); (c),(d) Co(3 nm)/W(6 nm); (e),(f) Co(3 nm)/Si(2 nm)/W(6 nm). Left figures are the THz waveform for front and back pumps, showing THz polarity reversal upon reversal of pump direction. Right figures are the emitted THz amplitudes versus magnetic field direction, showing onefold dependence. The data show that SCC is the mechanism of THz emission for all these samples.



absorbance spectra to establish whether the silicide is metallic or insulating. From the squared absorbance spectra, we extrapolate the data to the  $x$  axis, and read off the  $x$  intercept as the direct band gap as depicted in Fig. 3(a).

We see from Fig. 3(a) that the solid lines intersect the  $x$  axis at approximately 2 eV for  $d = 4 - 10$  nm [see also Fig. 3(b)], while for  $d = 2$  nm, the data is almost photon energy independent, and so cannot give a positive  $x$  intercept. Since this method of extracting the band gap is for a semiconductor, it suggests that Co(3 nm)/Si(2 nm) is no longer semiconducting, i.e., has become metallic. We also perform a control experiment, where we measure the absorbance spectra of pure Si layers (without Co). Figure 3(d) shows the direct band-gap ranges from approximately 2.7 eV for  $d = 2$  nm to approximately 2.1 eV for  $d = 10$  nm, consistent with quantum confinement effects [32]. From these two sets of absorbance data, we conclude that for the Co(3 nm)/Si( $d$ ) samples with thicker Si ( $d = 4 - 10$  nm), there is a coexistence of silicon and cobalt silicide, whereas in Co(3 nm)/Si(2 nm), the entire Si layer becomes metallic cobalt silicide. We further confirm our findings by performing reflectance ( $R$ ) and transmittance ( $T$ ) measurements of Co(3 nm)/Si( $d$ ) as shown in Figs. 4(a) and 4(b). By simultaneously fitting  $R(\omega)$  and  $T(\omega)$  to theoretical expressions corresponding to our heterostructure, we obtain the effective real and imaginary parts of the complex refractive index of the SiO<sub>2</sub>/Co/Si stack as illustrated in Figs. 4(c) and 4(d). We find that, for

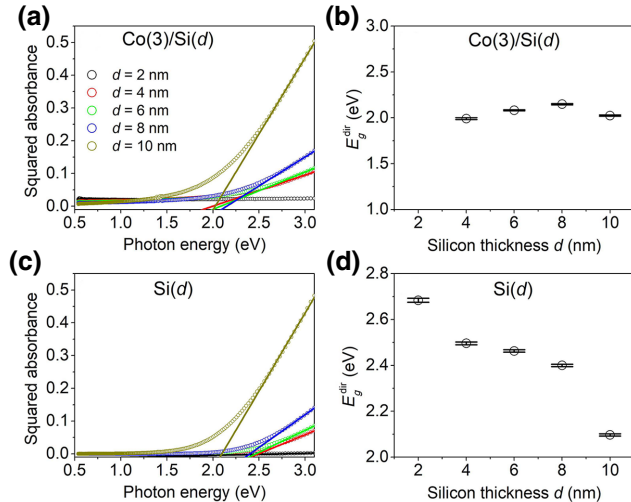


FIG. 3. Squared absorbance spectra for (a) Co(3 nm)/Si( $d$ ) and (c) Si( $d$ ), for  $d = 2, 4, 6, 8,$  and  $10$  nm. Circles represent data. Solid lines are the linear fit to high-energy response. For semiconductors, the intersection of the solid lines to the  $x$  axis gives the direct semiconductor band gap  $E_g^{\text{dir}}$ . (b) Extracted  $E_g^{\text{dir}}$  for different Si thicknesses. For Co(3 nm)/Si(2 nm), the squared absorbance is almost independent of energy and yields a negative band-gap value when fitted to the semiconductor expression. (d) For Si ( $d$ ), the extracted  $E_g^{\text{dir}}$  are all positive and ranges between 2.1–2.7 eV, agreeing with the literature.

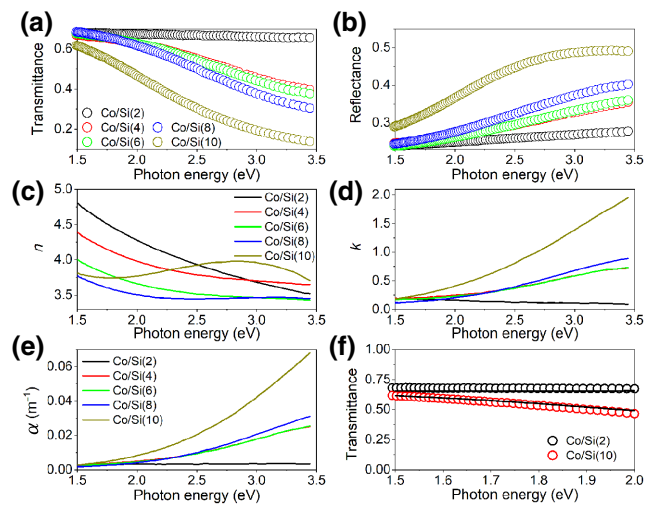


FIG. 4. Experimental (a) transmittance and (b) reflectance spectra for Co(3 nm)/Si( $d$ ). Calculated (c) real part  $n$  and (d) imaginary part  $\kappa$  of the complex refractive index, (e) absorption coefficient  $\alpha$ . (f) Experimental transmittance spectra for  $d = 2$  nm (black circle) and  $d = 10$  nm (red circle). Solid lines are fits to TMM (see the Supplemental Material [28]), showing that for  $d = 2$  nm, the best fit is obtained when all the Si is converted into CoSi, leading to a sample structure of approximately Co(1.9 nm)/CoSi(2.3 nm), whereas for  $d = 10$  nm, a good fit is also obtained when the same thickness of CoSi (approximately 2.3 nm) is formed, with the remaining Si having a thickness of approximately 8 nm.

$d = 4 - 10$  nm, the absorption coefficient  $\alpha$  increases with increasing frequency, while for 2 nm, and  $\alpha$  is frequency independent as depicted in Fig. 4(e). This analysis presents independent confirmation of our earlier result, that the Co(3 nm)/Si(2 nm) later is effectively metallic, suggesting that all the Si has become metallic silicide.

Having concluded that the formed silicide is metallic, we now proceed to estimate the thickness of the silicide layer and whether there is any surviving cobalt. To do this we assume the formation of only metallic CoSi, neglecting the formation of other silicides with different stoichiometries. Using molar mass and density of each material, we can conclude that, approximately, 1.0 nm of Co with 1.8 nm of Si will form 2.1 nm of CoSi. With  $x$  as the unknown amount (in nm) of Co converted to silicide, the sample structure is SiO<sub>2</sub>(3 nm)/Co(3- $x$  nm)/CoSi(2.087 $x$  nm)/Si( $d-1.822x$  nm)/quartz substrate(1 nm), where  $d = 2 - 10$  nm. We calculate the transmittance of the mentioned structure using a modified transfer matrix method (TMM) [33,34] based on existing dielectric constants [35–38] and fit it to the experimental measurements over a range of frequencies (details in the Supplemental Material [28]). The best fit for  $d = 2$  nm as shown in Fig. 4(f) is obtained when all Si is converted into CoSi, leading to a sample structure of approximately Co(1.9 nm)/CoSi(2.3 nm). For the other samples ( $d = 4 -$

10 nm), a good fitting is also obtained when the same thickness of CoSi (approximately 2.3 nm) is formed, with the remaining Si for each sample having thickness of approximately 2–8 nm, respectively. The results confirm that for  $d = 2$  nm sample all layers are conducting, while for  $d = 4 - 10$  nm there will be coexistence of silicon and cobalt silicide.

Since Si has very weak SOC and hence would not have emitted any measurable THz radiation, it is therefore reasonable to infer that the silicide layer is responsible for the SCC. We first perform a control experiment where we analyze the THz emission from Co(3 nm)/Pt(6 nm) and Co(3 nm)/W(6 nm) samples [see Figs. 2(a)–2(d)]. We confirm that the signal obtained is due to SCC [Fig. 2(f)] and that the sign of the spin Hall angle ( $\theta_{\text{SH}} = \mathbf{j}_c/\mathbf{j}_s$ ) of Pt and W are opposite [Figs. 2(a) and 2(c)] [16,19,39]. Next we sandwich a Si layer between Co and W to obtain Co(3 nm)/Si( $d$  nm)/W(6 nm) for  $d = 2 - 10$  nm. We observe that, when compared to emission from Co(3 nm)/W(6 nm), the polarity of the emitted THz flips for  $d = 2 - 10$  nm as shown in Fig. 5(a). If SCC were to occur inside the W layer in Co(3 nm)/Si( $d$  nm)/W(6 nm), we would not see any flipping of the THz polarity. Our data thus show SCC occurs inside the silicide layer, resulting in a strong THz emission.

Even though the THz emission from the Co(3 nm)/Si( $d$  nm)/W(6 nm) sample is reduced compared to the Co(3 nm)/Si(2 nm), it still maintains a comparable amplitude. Our TMM calculations show that the reduction can be justified by the absorption in the alternative metallic layer. Although we cannot completely exclude that some spin current reaches the W layer, it is also interesting to observe that the THz emission is constant for most of the Si thicknesses. This hints that the W here acts simply as a passive layer (simply absorbing part of the emitted THz) and its presence has not altered the main source of SCC. This implies that SCC must have happened at the Co/Si interface and therefore within the silicide layer.

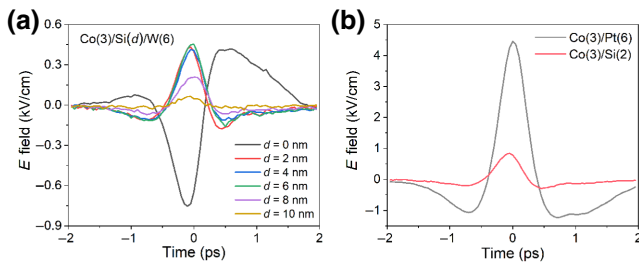


FIG. 5. (a) Emitted THz waveforms for Co (3 nm)/Si ( $d$  nm)/W (6 nm) for  $d = 0 - 10$  nm. The waveform at  $d = 0$  nm [i.e. Co (3 nm)/W (6 nm)] is opposite to waveforms for all non-zero values of  $d$ , suggesting that the Si layer prevents the spin current that is created in the Co layer from reaching the W layer. (b) Emitted THz waveforms of Co (3 nm)/Pt (6 nm) and Co (3 nm)/Si (2 nm), showing the Co/Si to be an efficient THz emitter.

Spin injection into silicon is typically carried out with a layer of oxide to prevent silicide formation [40]; however, the silicide layer would reduce the injection efficiency. As such, the SCC efficiency ( $\theta_{\text{SH}}$ ) in silicides has not been reported in the literature. To estimate  $\theta_{\text{SH}}$  in cobalt silicide, we compare the THz emission of Co(3 nm)/Si(2 nm) and Co(3 nm)/Pt(6 nm) under the simplifying assumption that the generated spin current at parity of absorbed laser fluence is the same in both samples. From Fig. 5(b), the peak THz emission from Co(3 nm)/Si(2 nm) is approximately 0.2 times that of Co(3 nm)/Pt(6 nm). Using the reported spin Hall angle of 0.068 in 6-nm-thick Pt [41] as well as the calculated excitation laser absorption and theoretical THz emission, the spin Hall angle in silicide is around  $\theta_{\text{SH}} = 0.016$  (details within the Supplemental Material [28]). This value of  $\theta_{\text{SH}}$  is not small compared to most other normal metals [42], suggesting that cobalt silicide is a strong emitter of THz radiation via SCC.

Considering the pivotal role that Si plays in bridging current electronics to next generation of spintronics, our work suggests that Co/Si is a promising material for spintronics devices. Furthermore, the peak THz electric field radiation is only slightly smaller than that from ZnTe (details in Supplemental Material [28]), which is traditionally used as a THz emission source. Compared to ZnTe, the simplicity of our heterostructure and the compatibility with Si-based electronics allows for easier integration with modern electronics.

#### IV. CONCLUSION

We perform THz emission measurements on Co(3 nm)/Si(2 nm), Co(3 nm)/Pt(6 nm), Co(3 nm)/W(6 nm) and Co(3 nm)/Si( $d$  nm)/W(6 nm). We produce a very efficient THz emitter with minimal complexity and directly integrated on silicon. Our data are consistent with SCC mechanism occurring at the Co/Si interface. Steady-state absorbance measurements suggest the Co/Si interface to be metallic in nature. The spin Hall angle of the silicide layer is estimated to be 0.016, which is quite significant, since it is of the same order of magnitude (approximately 20%) as that of the heavy metal Pt, which has large SOC and is widely thought to be a strong emitter of THz radiation.

#### ACKNOWLEDGMENTS

This work is supported by the Singapore Ministry of Education AcRF Tier 3 Programme “Geometrical Quantum Materials” (Grant No. MOE2018-T3-1-002), the Singapore National Research Foundation Competitive Research Programme “The Next Generation of Spintronics with 2D Heterostructures” (Grant No. NRF-CRP22-2019-0004), National Research Foundation Singapore Investigatorship (Grant No. NRFI06-2020-0015) and “AME-IRG through RIE2020 funds under Grant No.

A1983c0037". The electron microscopy and x-ray photoelectron spectroscopy works are performed at the Facility for Analysis, Characterization, Testing and Simulation (FACTS), Nanyang Technological University, Singapore. M.B. acknowledges Nanyang Technological University, Singapore, NAP-SUG.

- 
- [1] A. A. Melnikov, K. N. Boldyrev, Y. G. Selivanov, V. P. Martovitskii, S. V. Chekalin, and E. A. Ryabov, Coherent phonons in a  $\text{Bi}_2\text{Se}_3$  film generated by an intense single-cycle THz pulse, *Phys. Rev. B* **97**, 214304 (2018).
- [2] J. Kim, O.-P. Kwon, F. D. J. Brunner, M. Jazbinsek, S.-H. Lee, and P. Günter, Phonon modes of organic electro-optic molecular crystals for terahertz photonics, *J. Phys. Chem. C* **119**, 10031 (2015).
- [3] J.-H. Son, S. J. Oh, and H. Cheon, Potential clinical applications of terahertz radiation, *J. Appl. Phys.* **125**, 190901 (2019).
- [4] H. Chen, W.-J. Lee, H.-Y. Huang, C.-M. Chiu, Y.-F. Tsai, T.-F. Tseng, J.-T. Lu, W.-L. Lai, and C.-K. Sun, Performance of THz fiber-scanning near-field microscopy to diagnose breast tumors, *Opt. Express* **19**, 19523 (2011).
- [5] M. A. Huber, F. Mooshammer, M. Plankl, L. Viti, F. Sandner, L. Z. Kastner, T. Frank, J. Fabian, M. S. Vitiello, T. L. Cocker, and R. Huber, Femtosecond photo-switching of interface polaritons in black phosphorus heterostructures, *Nat. Nanotechnol.* **12**, 207 (2017).
- [6] J. Zhang, X. Chen, S. Mills, T. Ciavatti, Z. Yao, R. Mescall, H. Hu, V. Semenenko, Z. Fei, H. Li, V. Perebeinos, H. Tao, Q. Dai, X. Du, and M. Liu, Terahertz nanoimaging of graphene, *ACS Photonics* **5**, 2645 (2018).
- [7] L. Cheng, X. Wang, W. Yang, J. Chai, M. Yang, M. Chen, Y. Wu, X. Chen, D. Chi, K. E. J. Goh, J.-X. Zhu, H. Sun, S. Wang, J. C. W. Song, M. Battiato, H. Yang, and E. E. M. Chia, Far out-of-equilibrium spin populations trigger giant spin injection into atomically thin  $\text{MoS}_2$ , *Nat. Phys.* **15**, 347 (2019).
- [8] S. Kovalev, K.-J. Tielrooij, J.-C. Deinert, I. Ilyakov, N. Awari, M. Chen, A. Ponomaryov, M. Bawatna, T. V. A. G. de Oliveira, L. M. Eng, K. A. Kuznetsov, D. A. Safrotenkov, G. K. Kitaeva, P. I. Kuznetsov, H. A. Hafez, D. Turchinovich, and M. Gensch, Terahertz signatures of ultrafast Dirac fermion relaxation at the surface of topological insulators, *Npj Quantum Mater.* **6**, 84 (2021).
- [9] X. Wang, L. Cheng, D. Zhu, Y. Wu, M. Chen, Y. Wang, D. Zhao, C. B. Boothroyd, Y. M. Lam, J.-X. Zhu, M. Battiato, J. C. W. Song, H. Yang, and E. E. M. Chia, Ultrafast spin-to-charge conversion at the surface of topological insulator thin films, *Adv. Mater.* **30**, 1802356 (2018).
- [10] J.-H. Shim, A. A. Syed, J.-I. Kim, H.-G. Piao, S.-H. Lee, S.-Y. Park, Y. S. Choi, K. M. Lee, H.-J. Kim, J.-R. Jeong, J.-I. Hong, D. E. Kim, and D.-H. Kim, Role of non-thermal electrons in ultrafast spin dynamics of ferromagnetic multilayer, *Sci. Rep.* **10**, 6355 (2020).
- [11] Y. Zhang, K. Li, and H. Zhao, Intense terahertz radiation: Generation and application, *Front. Optoelectron.* **14**, 4 (2021).
- [12] H. Lin and C. P. Liu, Terahertz radiation generation from metallic electronic structure manipulated by inhomogeneous DC-fields, *Sci. Rep.* **11**, 6663 (2021).
- [13] M. Naftaly, N. Vieweg, and A. Deninger, Industrial applications of terahertz sensing: State of play, *Sensors* **19**, 4203 (2019).
- [14] R. I. Stantchev, X. Yu, T. Blu, and E. Pickwell-MacPherson, Real-time terahertz imaging with a single-pixel detector, *Nat. Commun.* **11**, 2535 (2020).
- [15] L. Yu, L. Hao, T. Meiqiong, H. Jiaoqi, L. Wei, D. Jinying, C. Xueping, F. Weiling, and Z. Yang, The medical application of terahertz technology in non-invasive detection of cells and tissues: Opportunities and challenges, *RSC Adv.* **9**, 9354 (2019).
- [16] T. Seifert *et al.*, Efficient metallic spintronic emitters of ultrabroadband terahertz radiation, *Nat. Photonics* **10**, 483 (2016).
- [17] T. Kampfrath, M. Battiato, P. Maldonado, G. Eilers, J. Nötzold, S. Mährlein, V. Zbarsky, F. Freimuth, Y. Mokrousov, S. Blügel, M. Wolf, I. Radu, P. M. Oppeneer, and M. Münzenberg, Terahertz spin current pulses controlled by magnetic heterostructures, *Nat. Nanotechnol.* **8**, 256 (2013).
- [18] E. T. Papaioannou and R. Beigang, THz spintronic emitters: A review on achievements and future challenges, *Nanophotonics* **10**, 1243 (2021).
- [19] Y. Wu, M. Elyasi, X. Qiu, M. Chen, Y. Liu, L. Ke, and H. Yang, High-performance THz emitters based on ferromagnetic/nonmagnetic heterostructures, *Adv. Mater.* **29**, 1603031 (2017).
- [20] M. Chen, Y. Wu, Y. Liu, K. Lee, X. Qiu, P. He, J. Yu, and H. Yang, Current-enhanced broadband THz emission from spintronic devices, *Adv. Opt. Mater.* **7**, 1801608 (2019).
- [21] S. Thomas, Germanium nanowire transistors stack up, *Nat. Electron.* **4**, 452 (2021).
- [22] J. D. Plummer, M. D. Deal, and P. B. Griffin, *Silicon VLSI Technology: Fundamentals, Practice and Modeling* (Prentice-Hall, Englewood Cliffs, NJ, 2000).
- [23] X. Chen and C. Liang, Transition metal silicides: Fundamentals, preparation and catalytic applications. Metal silicides: An integral part of microelectronics, *Catal. Sci. Technol.* **9**, 4785 (2019).
- [24] L. J. Chen, Effect of annealing on magnetic properties and silicide formation at Co/Si interface, *JOM* **57**, 24 (2005).
- [25] S. Agarwal, V. Ganesan, A. K. Tyagi, and I. P. Jain, Effect of annealing on magnetic properties and silicide formation at Co/Si interface, *Bull. Mater. Sci.* **29**, 647 (2006).
- [26] M. V. Gomoyunova, G. S. Grebenyuk, I. I. Pronin, S. M. Solov'ev, O. Vilkov, and D. V. Vyalykh, Formation and magnetic properties of the silicon-cobalt interface, *Phys. Solid State* **55**, 437 (2013).
- [27] H. A. Hafez, X. Chai, A. Ibrahim, S. Mondal, D. Férachou, X. Ropagnol, and T. Ozaki, Intense terahertz radiation and their applications, *J. Opt.* **18**, 093004 (2016).
- [28] See Supplemental Material at <http://link.aps.org/supplemental/10.1103/PhysRevApplied.18.034056> for details on electric field strength estimation, composition characterizations, magnetic characterizations, transfer matrix method, theoretical calculations, and some other

- problems involved in the text, which includes Refs. [7,33,34,37,43–47].
- [29] M. Battiato, K. Carva, and P. M. Oppeneer, Superdiffusive Spin Transport as a Mechanism of Ultrafast Demagnetization, *Phys. Rev. Lett.* **105**, 027203 (2010).
- [30] M. Battiato, K. Carva, and P. M. Oppeneer, Theory of laser-induced ultrafast superdiffusive spin transport in layered heterostructures, *Phys. Rev. B* **86**, 024404 (2012).
- [31] L. Cheng, Z. Li, D. Zhao, and E. E. M. Chia, Studying spin–charge conversion using terahertz pulses, *APL Mater.* **9**, 070902 (2021).
- [32] H. V. Nguyen, Y. Lu, S. Kim, M. Wakagi, and R. W. Collins, Optical Properties of Ultrathin Crystalline and Amorphous Silicon Films, *Phys. Rev. Lett.* **74**, 3880 (1995).
- [33] Y. Yang, S. Dal Forno, and M. Battiato, Removal of spectral distortion due to echo for ultrashort THz pulses propagating through multilayer structures with thick substrate, *J. Infrared Millim. Terahertz Waves* **42**, 1142 (2021).
- [34] Y. Yang, S. Dal Forno, and M. Battiato, Transfer-matrix description of heterostructured spintronics terahertz emitters, *Phys. Rev. B* **104**, 155437 (2021).
- [35] L. Gao, F. Lemarchand, and M. Lequime, Exploitation of multiple incidences spectrometric measurements for thin film reverse engineering, *Opt. Express* **20**, 15734 (2012).
- [36] P. B. Johnson and R. W. Christy, Optical constants of the noble metals, *Phys. Rev. B* **9**, 5056 (1974).
- [37] Z. Ni, K. Wang, Y. Zhang, O. Pozo, B. Xu, X. Han, K. Manna, J. Paglione, C. Felser, A. G. Grushin, F. de Juan, E. J. Mele, and L. Wu, Giant topological longitudinal circular photo-galvanic effect in the chiral multifold semimetal CoSi, *Nat. Commun.* **12**, 154 (2021).
- [38] D. T. Pierce and W. E. Spicer, Electronic structure of amorphous Si from photoemission and optical studies, *Phys. Rev. B* **5**, 3017 (1972).
- [39] T. S. Seifert, N. M. Tran, O. Gueckstock, S. M. Rouzgar, L. Nadvornik, S. Jaiswal, G. Jakob, V. V. Temnov, M. Muenzenberg, M. Wolf, M. Kläui, and T. Kampfrath, Terahertz spectroscopy for all-optical spintronic characterization of the spin-Hall-effect metals Pt, W and Cu<sub>80</sub>Ir<sub>20</sub>, *J. Phys. D: Appl. Phys.* **51**, 364003 (2018).
- [40] B. T. Jonker, G. Kioseoglou, A. T. Hanbicki, C. H. Li, and P. E. Thompson, Electrical spin-injection into silicon from a ferromagnetic metal/tunnel barrier contact, *Nat. Phys.* **3**, 542 (2007).
- [41] Y. Wang, P. Deorani, X. Qiu, J. H. Kwon, and H. Yang, Determination of intrinsic spin Hall angle in Pt, *Appl. Phys. Lett.* **105**, 152412 (2014).
- [42] Y. Niimi and Y. Otani, Reciprocal spin Hall effects in conductors with strong spin–orbit coupling: A review, *Rep. Prog. Phys.* **78**, 124501 (2015).
- [43] H. H. Li, Refractive index of ZnS, ZnSe, and ZnTe and its wavelength and temperature derivatives, *J. Phys. Chem. Ref. Data* **13**, 103 (1984).
- [44] S. L. Dexheimer, *Terahertz Spectroscopy: Principles and Applications* (CRC Press, Boca Raton, 2007).
- [45] P. C. M. Planken, H.-K. Nienhuys, H. J. Bakker, and T. Wenckebach, Measurement and calculation of the orientation dependence of terahertz pulse detection in ZnTe, *J. Opt. Soc. Am. B* **18**, 313 (2001).
- [46] H. Seo, H. Yang, Y. Yang, K. Kim, S. Kim, H. Lee, and J. Kim, Scalable synthesis and electrochemical properties of porous Si-CoSi<sub>2</sub>-C composites as an anode for Li-ion batteries, *Materials* **14**, 5397 (2021).
- [47] M. A. Ordal, R. J. Bell, R. W. Alexander, L. L. Long, and M. R. Querry, Optical properties of fourteen metals in the infrared and far infrared: Al, Co, Cu, Au, Fe, Pb, Mo, Ni, Pd, Pt, Ag, Ti, V, and W, *Appl. Opt.* **24**, 4493 (1985).